Aggregate

WILEY

Aggregate Open Access

RESEARCH ARTICLE OPEN ACCESS

Well-Designed Organic Semiconductors With Tunable Resistive Switching Behaviors for Multilevel Storage and Neuromorphic Computing

Dehui Wang[1] | Jinxiang Yin[1] | Yuexin Li[1] | Hongmin Li[1] | Min Wang[1] | Feng Guo[2] | Wenjing Jie[1] | Feijie Song[1] | Jianhua Hao[2]

[1]College of Chemistry and Materials Science, Sichuan Normal University, Chengdu, China | [2]Department of Applied Physics, The Hong Kong Polytechnic University, Hong Kong, China

Correspondence: Wenjing Jie (wenjing.jie@sicnu.edu.cn) | Feijie Song (fsong@sicnu.edu.cn) | Jianhua Hao (jh.hao@polyu.edu.hk)

Received: 29 March 2025 | **Revised:** 11 June 2025 | **Accepted:** 29 June 2025

Funding: This work was supported by the grants from the National Natural Science Foundation of China (No. 62474118, 52233014, and 62411560160), the Sichuan Science and Technology Program (No. 2022ZYD0041), and the PolyU grants (1-W22S and 1-CE0H).

Keywords: multilevel storage | neuromorphic computing | organic semiconductors | resistive switching | thin films

ABSTRACT

Designing new materials with high-performance resistive switching (RS) behaviors and/or developing alternative means to modulate the RS behaviors are of great significance for information storage and neuromorphic computing. Herein, we present a novel strategy to design and synthesize furan-annulated naphthalenes for high-performance digital and analog RS behaviors through controlling substituents. By introducing an electron acceptor of trifluoromethyl on the phenyl ring, 3-phenyl-4-(4-trifluoromethylphenyl)-2*H*-naphtho[1,8-*bc*]furan (TPNF) is synthesized with donor–acceptor (D–A) pairs by utilizing the electron donor of furyl in the naphthalene. Owing to the constructed D–A systems where electrons can be transported under the external bias voltage, the prepared TPNF thin films demonstrate high-performance bipolar digital RS behaviors with multilevel storage characteristics. On the other hand, if the substituent on the phenyl ring is replaced by an electron donor of methoxy, 4-(4-methoxyphenyl)-3-phenyl-2*H*-naphtho[1,8-*bc*]furan (MPNF) can be constructed with only electron-donor units of furyl and methoxy. The fabricated MPNF thin films show analog RS behaviors owing to the carrier trapping/detrapping from the nucleophilic trapping sites generated from the electron-donor units. The analog memristors demonstrate synaptic functions with high linearity of conductance modulation, which is highly desirable for neuromorphic computing. Such synaptic memristors based on MPNF are completely capable of recognizing digit images with high accuracy (95.2%) and implementing decimal arithmetic of addition, subtraction, multiplication, and division operations. This study provides a feasible way to modulate the RS properties by the strategy of introducing different substituents, demonstrating promising applications of such well-designed organic semiconductors for multilevel storage and neuromorphic computing.

Dehui Wang and Jinxiang Yin contributed equally to this work.

1 | Introduction

Memristor with tunable resistive switching (RS) properties is one of the most promising candidates for applications in digital information storage and logic operations as well as neuromorphic computing [1, 2]. It would be important and also meaningful to explore potential materials with suitable RS properties and synaptic functions. At present, numerous inorganic and organic functional materials have been employed to serve as the RS layer in diverse memristive devices [3–5]. In recent years, many flexible and wearable electronic devices have drawn much attention due to the increasing demand for biocompatible applications [6, 7]. Memristors with good flexibility and biocompatibility are highly desirable. Compared with their inorganic counterparts, organic materials have tremendous advantages in memristive devices owing to their good biocompatibility, mechanical flexibility, low-temperature manufacturing, and molecular group modifiability [8–10]. And more importantly, the geometry and structures, as well as the electrical properties of the organic materials, can be well tuned through rational design of molecules and development of synthetic strategy, which provides more potential for applications in memristive devices for information storage and artificial intelligence.

During the past few years, some important achievements have been reported in memristors based on organic materials [11, 12]. The conductivity of organic materials can be controlled or modified by charge transfer and redox activities in memristors, where digital RS with a large ON/OFF ratio can be achieved [13]. For such redox activities, donor–acceptor (D–A) pairs should typically be designed with electron donor and acceptor units to construct the D–A systems, where electrons are prone to be generated and transported to achieve intrinsic RS behaviors [8, 14]. For example, in 2022, Tao et al., reported the electrochemical preparation of carbazole-based porous organic polymer films with a D–A system by using the carbazole unit as the donor and the cyano group as the acceptor for applications in memristive devices [15]. However, in this case, the memristors generally demonstrate digital RS with a high switching ratio [16, 17]. On the other hand, analog RS behaviors with a series of tunable resistance states are more suitable for artificial synaptic devices and future neuromorphic computing [18, 19]. Therefore, the design of new materials with tunable RS behaviors and/or developing alternative means to modulate RS behaviors are of great significance for memristors to meet the needs of different applications.

Herein, we present a novel design strategy to achieve digital RS behaviors for multilevel storage or analog RS behaviors for synaptic through introducing different substituents to serve as electron acceptors or donors. Recently, we developed an Rh-catalyzed intramolecular annulation of O-bearing alkyne-tethered benzocyclonovel for the synthesis of furan-annulated naphthalenes via C—C bond activation [20]. By using this protocol, naphthalenes with electron-rich and/or -deficient aryl groups can be easily synthesized in a regio-controlled manner, which may offer a good platform to explore various RS behaviors. As a proof of concept, we design and synthesize two organic semiconductors. By introducing an electron acceptor of trifluoromethyl on the phenyl ring, 3-phenyl-4-(4-trifluoromethylphenyl)-2*H*-naphtho[1,8-*bc*]furan (TPNF) is synthesized with D–A pairs by utilizing the electron donor of furyl in the naphthalene. On the other hand, if the substituent on the phenyl ring is replaced by an electron donor of methoxy, 4-(4-methoxyphenyl)-3-phenyl-2*H*-naphtho[1,8-*bc*]furan (MPNF) can be constructed with only electron-donor units of furyl and methoxy. The TPNF with D–A pairs by using the trifluoromethyl as an electron acceptor and the furyl as a donor demonstrates typical non-volatile bipolar digital RS behaviors and multilevel storage characteristics. While the MPNF with only electron donors of furyl and methoxy demonstrates analog RS behaviors and good synaptic functions of paired-pulse facilitation (PPF) and paired-pulse depression (PPD), as well as long-term potentiation (LTP) and long-term depression (LTD), with high linearity of conductance modulation. Furthermore, simulation results demonstrate that the synaptic memristors are completely capable of recognizing digit images with high accuracy and performing decimal arithmetic of addition, subtraction, multiplication, and division operations. This study indicates that substituents in well-designed organic semiconductors can be used as an additional degree of freedom to control the RS behaviors for applications in multilevel storage and neuromorphic computing.

2 | Results and Discussion

The organic semiconductors are well designed and synthesized by using 1.0 mol% $[Rh(cod)OH]_2$ as the catalyst and 1.5 equiv. $ZnCl_2$ as the Lewis acid (see Figure S1 and Section 4 for more synthesis details). Then, the organic thin films can be deposited on SiO_2/Si substrates for characterization and on the indium tin oxide-coated polyethylene terephthalate (ITO/PET) for device fabrication by the thermal evaporation method, as schematically shown in Figure 1a. The synthesized organic materials are characterized by ^{1}H nuclear magnetic resonance (NMR) spectroscopy, as shown in Figure 1b. The specific peak analysis is shown in Figure S2, suggesting the successful synthesis of the two types of organic materials. Figure 1c shows the ultraviolet-visible (UV–VIS) absorption spectrum of the two materials. The two absorption peaks located at 212 and 270 nm may be caused by π–π^* transitions [21, 22], while the weak absorption peak at 339 nm may be attributed to n–π^* transitions [23]. According to the UV–VIS absorption spectrum, the bandgap of TPNF and MPNF can be calculated to be 3.20 and 3.21 eV, respectively, as shown in Figure S3. In addition, ultraviolet photoelectron spectroscopy (UPS) has been used to detect the synthesized materials, as shown in Figure S4. The highest occupied molecular orbital (HOMO) energy level of −5.87 eV (−5.86 eV) can be estimated from the UPS spectrum, and the lowest unoccupied molecular orbital (LUMO) energy level of TPNF (MPNF) can be calculated to be −2.67 eV (−2.65 eV) according to the equation of $E_{LUMO} = E_{HOMO} + E_g$ (E_{HOMO} and E_{LUMO} are the HOMO and LUMO energy levels, respectively, and E_g is the bandgap of TPNF or MPNF). Furthermore, quantum-chemical geometry optimization of density functional theory (DFT) at the B3LYP level with 6–31G basis functions has been used to validate the observed differences in HOMO/LUMO levels and electronic distributions between TPNF and MPNF, as shown in Figure S5. The HOMO and LUMO levels can be calculated by using the B3LYP/6-31G level of DFT calculations, as shown in Table S1, suggesting that the HOMO and LUMO levels calculated using UPS and UV–VIS absorption spectra are reliable. Figure 1d demonstrates X-ray diffraction (XRD) patterns of the

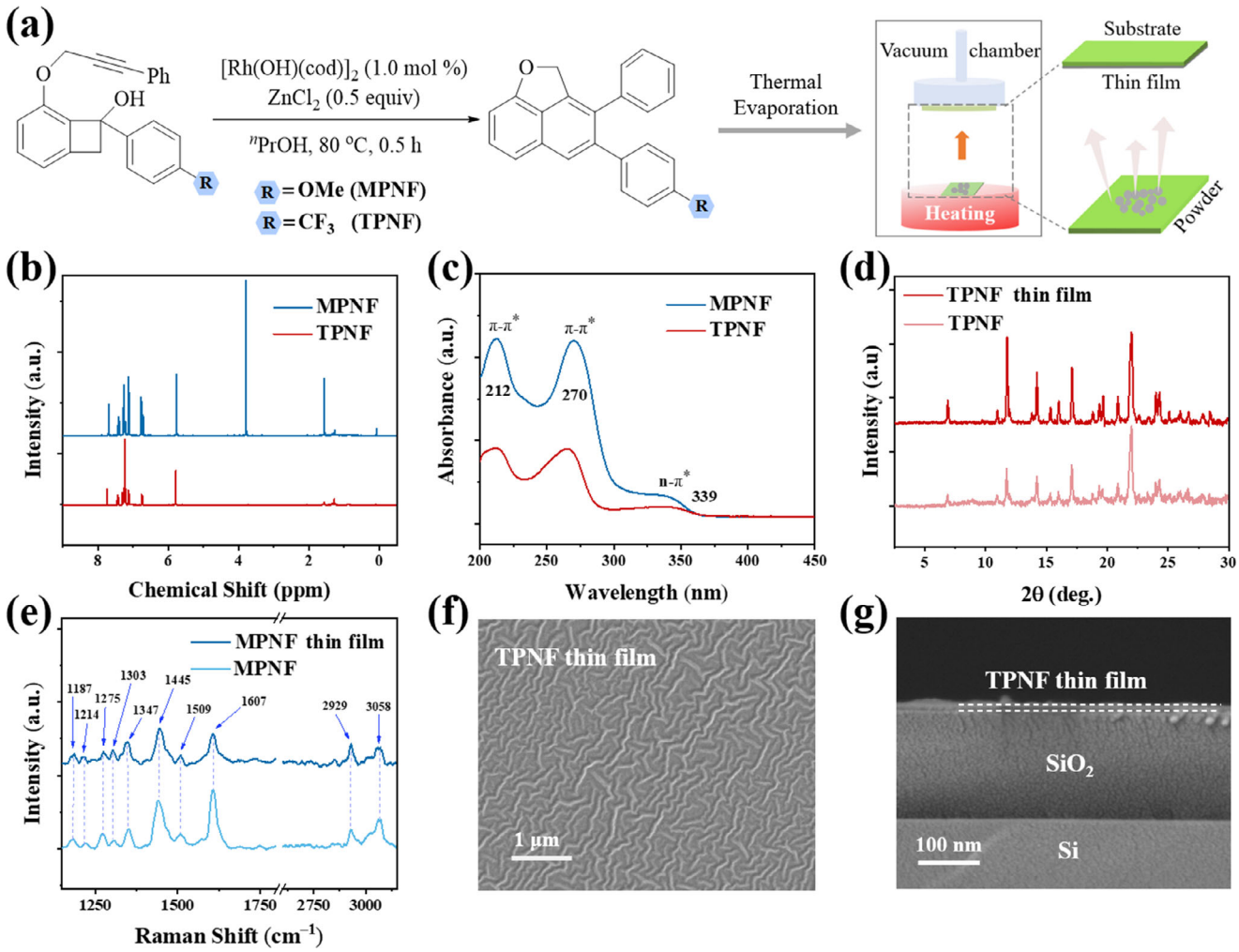

FIGURE 1 | Characterization of the synthesized organic semiconductor of TPNF and MPNF. (a) Synthesis process and preparation of thin film by thermal evaporation. (b) ^{1}H NMR spectra of TPNF and MPNF. (c) UV–VIS absorption spectra of TPNF and MPNF. (d) XRD patterns of TPNF and TPNF thin film. (e) Raman spectra of MPNF and MPNF thin film. (f) Surface morphology of the SEM image for the TPNF thin film. (g) Cross-sectional SEM image of TPNF thin film deposited on SiO_2/Si substrate.

synthesized TPNF and the deposited thin film. All the observed diffraction peaks of the thin film are consistent with those of the bulk materials, indicating the successful preparation of the thin films. Figure 1e shows the Raman spectra of the synthesized MPNF and the deposited thin films. Among them, the Raman feature peaks at 3058 and 2929 and 1187 cm^{-1} correspond to the phenyl ring C—H vibration mode of symmetrical stretching, anti-symmetrical stretching, and shear vibration mode, respectively [24]. The Raman peak at 1607 cm^{-1} may arise from the phenyl ring C═C bending vibration mode [25]. The peak located at 1275 cm^{-1} may represent the C—O stretching vibration mode, suggesting the existence of —OCH_3 [25] The peak located at 1214 cm^{-1} may result from the symmetric stretching of C—O—C from the furan [26] All the Raman feature peaks observed in the thin film are well consistent with those in the bulk, suggesting the MPNF thin film has been well deposited on SiO_2/Si substrates. The atomic force microscopy (AFM) technique has been employed to characterize the surface morphology and determine the topographical uniformity of the organic thin films (Figure S6), exhibiting the synthesized continuous and uniform thin films. The scanning electron microscope (SEM) is also used to determine the thickness of the as-prepared TPNF thin film on the SiO_2/Si substrate, as shown in Figure 1g. The thickness of the deposited film is about 20 nm. All the aforementioned data show that the TPNF and MPNF thin films can be successfully prepared by the thermal evaporation method.

In order to explore the memristive properties, the organic thin films are deposited on ITO-coated PET substrate, and two-terminal memristors with Pt as the top electrode and ITO as the bottom electrode are fabricated. As shown in Figure 2a, TPNF demonstrates non-volatile bipolar digital RS behaviors with a typical current–voltage (I–V) characteristic curve where a sharp current transition can be observed from the high resistance state (HRS) to low resistance states (LRS) at the SET voltage of 0.55 V and from the HRS to the HRS at the RESET voltage of 0.51 V, respectively. The fabricated device demonstrates good environmental stability. After 1 month, the device still exhibits comparable bipolar RS behaviors without obvious degradation, as shown in Figure 2b. Moreover, the cycle-to-cycle variations for the TPNF memristor are shown in Figure S7. All the I–V curves demonstrate typical bipolar digital RS behaviors with very

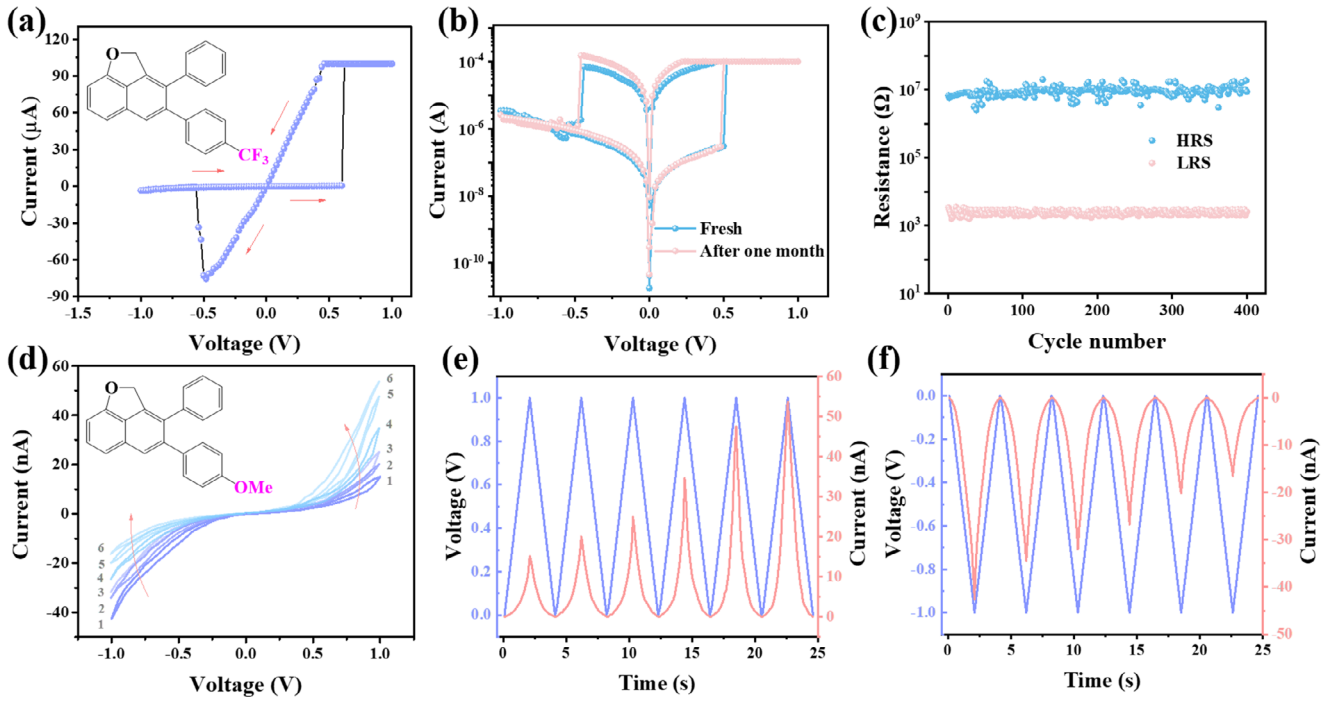

FIGURE 2 | RS behaviors of TPNF and MPNF. (a) Typical digital RS behavior of TPNF-based memristor. The inset shows the molecular structure of TPNF. (b) *I*–*V* curves of fresh TPNF memristor and device after being stored in air for one month. (c) Endurance characteristics of the memristor at a read voltage of 0.02 V. (d) Typical analog RS behavior of MPNF-based memristor. The current and voltage data as a function of time for the six consecutive cycles at both positive (e) and negative voltages (f).

close SET and RESET voltages. Figure 2c exhibits the endurance characteristics of the memristor by applying a pulse voltage of 0.8 and −1 V at a read voltage of 0.02 V. The device can realize write and erase operations for 400 cycles with a high ON/OFF the ratio up to 10^4, indicating good endurance characteristics. On the other hand, MPNF demonstrates the non-volatile analog RS behaviors, as shown in Figure 2d. A slight current loop can be observed without an abrupt transition, suggesting the analog RS behaviors. When a series of consecutive voltage scanning circles of $0 \rightarrow 1 \rightarrow 0$ V or $0 \rightarrow -1 \rightarrow 0$ V are performed, the current shows a gradient change with a gradual potentiation or depression trend, as respectively shown in Figure 2e,f. Furthermore, the RS behaviors of 30 memristors based on MPNF thin films are measured to examine the cell-to-cell uniformity, as shown in Figure S8. All 30 memristors demonstrate comparable analog RS behaviors with slight current loops, suggesting good cell-to-cell uniformity for the MPNF devices. Such analog RS is desirable for the simulation of biological synapses.

The underlying physical mechanism for the two types of RS behaviors should be well explored. The observed non-volatile bipolar digital RS behaviors with the SET voltage of 0.55 V and ON/OFF ratio up to 10^4 in the TPNF mainly generate from the formed D–A pairs in the organic semiconductor, where the furyl in the naphthalene can work as the electron donor and trifluoromethyl on the phenyl ring can serve as the electron acceptor. In the D–A systems, the electrons are prone to be generated and transported when the bias voltage is in excess of the SET voltage to achieve intrinsic RS behaviors, giving rise to the observed digital RS. Similar digital RS behaviors have been reported in previous studies. [8, 14] On the other hand, in the organic semiconductor of MPNF, the D–A system cannot be constructed due to the absence of an electron-acceptor unit. Considering the barrier between the Pt (work function of −5.65 eV) and the HOMO level (−5.86 eV) of MPNF is smaller than that between Pt and the LUMO level (−2.65 eV), the positive carriers of the hole may be injected from the electrode to the MPNF thin film when an external electric field is applied [27]. Moreover, Figure S9 shows the transport properties of the MPNF thin film, suggesting *p*-type transport characteristics. Thus, the carriers in the MPNF are dominated by the holes. Herein, the RS mechanism is considered to be associated with charge trapping/detrapping. In the MPNF, the electron-donor units of methoxy and furyl groups can serve as nucleophilic trapping sites [28], giving rise to hole trapping and detrapping when stimulated by the external voltages. Initially, there are nucleophilic trapping sites randomly located in the MPNF. When positive voltages are applied, the nucleophilic trapping sites can be filled with holes. Thus, the subsequently injected holes can be transported more freely, resulting in a decrease in the resistance of the MPNF. When negative voltages are used, the holes filled in trapping sites are detrapped, inducing the potential well for the migration of the charge carrier as well as the increase in resistance of the MPNF.

Furthermore, the resistance states of fabricated memristors based on TPNF thin films can be tuned by the compliance current (I_{CC}) in the positive voltage sweeping ranging from 20 to 800 μA, as shown in Figure 3a. For each I_{CC}, non-volatile bipolar RS behavior can be obtained, and more importantly, we can achieve four different LRSs. Figure 3b illustrates the retention performance of the HRS and four LRSs at each I_{CC} at a read voltage of 0.02 V. The five resistance states can be clearly distinguished and maintained without obvious degradation for 10,000 s. And more importantly, there are no overlaps between the different resistance states,

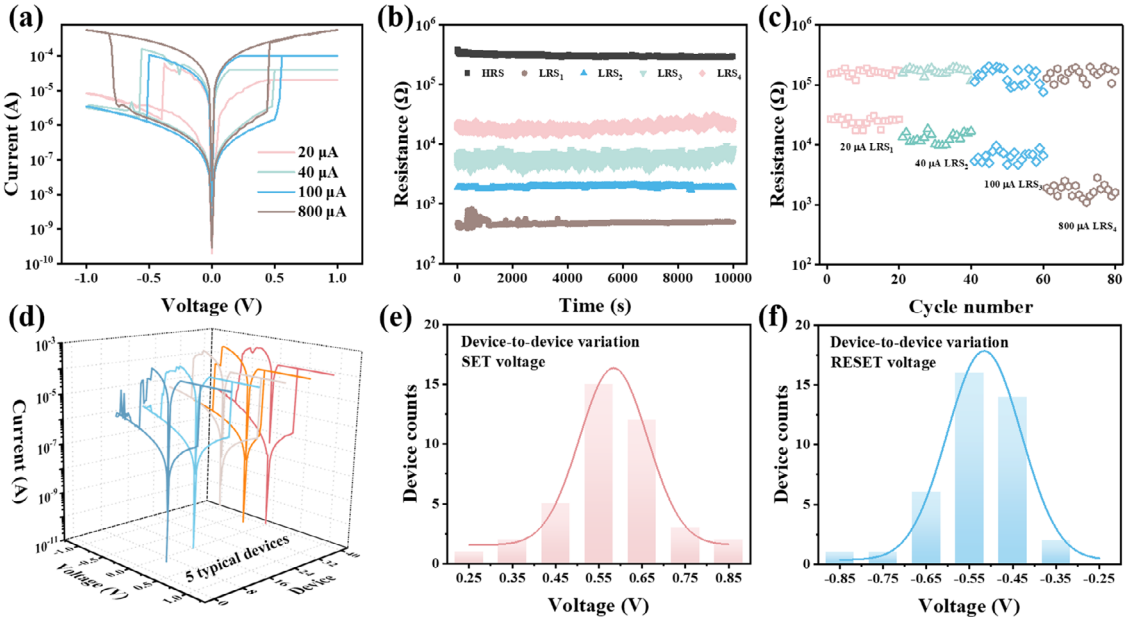

FIGURE 3 | Digital RS behaviors of the TPNF memristor. (a) Typical bipolar I–V curves with different I_{CC} ranging from 20 to 800 μA. (b) Retention stability of the HRS and four LRS at each I_{CC} at a read voltage of 0.02 V. (c) Switching endurance performance in pulse mode of HRS and LRS at each I_{CC} for 20 cycles. (d) The I–V curves of five typical memristors from 40 devices. The distribution of SET (e) and RESET (f) voltages of the 40 devices.

indicating the potential applications in multilevel storage. Figure 3c shows the endurance behaviors of the HRS and four LRS at each I_{CC} for 20 cycles. There are no obvious fluctuations for the HRS and LRS at each I_{CC} for 20 cycles. Such retention and endurance characteristics demonstrate the potenial applications in multilevel storage for the TPNF memristors. [29, 30] Besides, the TPNF thin film shows homogeneous RS behaviors with little device-to-device variation. Figure 3d shows the I–V characteristic curves of five typical memristors from 40 devices, and the RS behaviors of an additional 35 memristors are shown in Figure S10. All 40 devices demonstrate typical bipolar digital RS behaviors. The statistical results of the SET and RESET voltages about the 40 devices based on the TPNF films are shown in Figure 3e,f, respectively. The average value of SET (RESET) voltages is 0.58 V (−0.53 V), suggesting the homogeneous RS behaviors for the TPNF thin films. All these RS measurements suggest that the TPNF with D–A pairs can exhibit bipolar digital RS behaviors with a high ON/OFF ratio, and the LRS can be tuned by the I_{CC}, indicating multilevel storage characteristics.

On the other hand, artificial synapses can be achieved by utilizing the fabricated MPNF memristors with analog RS behaviors, where the conductance changes of the organic thin film can be used to represent the synaptic plasticity [31]. As schematically shown in Figure 4a, two neurons are interconnected by the synapse, which consists of the presynaptic membrane, synaptic cleft, and postsynaptic membrane [32]. The synaptic plasticity can be divided into short-term plasticity of PPF and PPD and long-term plasticity of LTP and LTD [33]. Among them, PPF demonstrates the enhancement of synaptic current response to the second pulse compared with the first one, while PPD represents the depression of that. Figure 4b shows the PPF index triggered by two consecutive pulses with positive voltage ($V = 4$ V, $W = 0.3$ s, where V stands for pulse voltage and W for pulse width) with different pulse intervals (Δt). The PPF index is defined as $[(A_2 - A_1)/A_1] \times 100\%$, where A_1 and A_2 are the synaptic current responses to the first and second pulse, respectively [34]. For PPF, A_2 is higher than A_1 owing to the potentiation stimulated by the positive pulses. The PPF index decreases exponentially with the pulse intervals. PPD can be stimulated by two consecutive pulses with negative voltage ($V = -4$ V, $W = 0.3$ s), as shown in Figure 4c. For PPD, A_2 is lower than A_1 due to the depression stimulated by the negative pulses. The PPD index decays with pulse intervals, indicating that the increased pulse intervals can reduce the depression effect. The simulated PPF and PPD behaviors are consistent with those of the biological synapses [35].

Furthermore, long-term plasticity LTP and LTD functions can be implemented based on the MPNF memristors, as shown in Figure 4d. A total of 20 sequential positive pulses (V = 4 V, W = 0.3 s, and Δt = 0.3 s) are used to implement the LTP functions with the conductance increased from 0.95 to 1.80 nS. In contrast, 20 sequential negative pulses ($V = -4$ V, $W = 0.3$ s, and Δt = 0.3 s) are employed for the LTD functions with the conductance reduced to 0.96 nS. Moreover, the LTP and LTD functions of a typical device are examined at different times, as shown in Figure S11. The device can maintain comparable LTP and LTD even after 90 days, suggesting good stability. To evaluate the linearity of the weight update in both the LTP and LTD processes, the changes in conductance of LTP (G_{LTP}) and LTD (G_{LTD}) with the pulse number (x) can be expressed by Equations 1 and 2, respectively [36].

$$G_{LTP}(x) = \frac{G_{max} - G_{min}}{1 - exp(-A_P)} \left[1 - exp\left(\frac{-A_P}{P_{max}} \times x\right)\right] + G_{min} \quad (1)$$

$$G_{LTD}(x) = \frac{G_{max} - G_{min}}{1 - exp(-A_D)} \left\{1 - exp\left[\frac{-A_D}{P_{max}} \times (2P_{max} - x)\right]\right\} + G_{min} \quad (2)$$

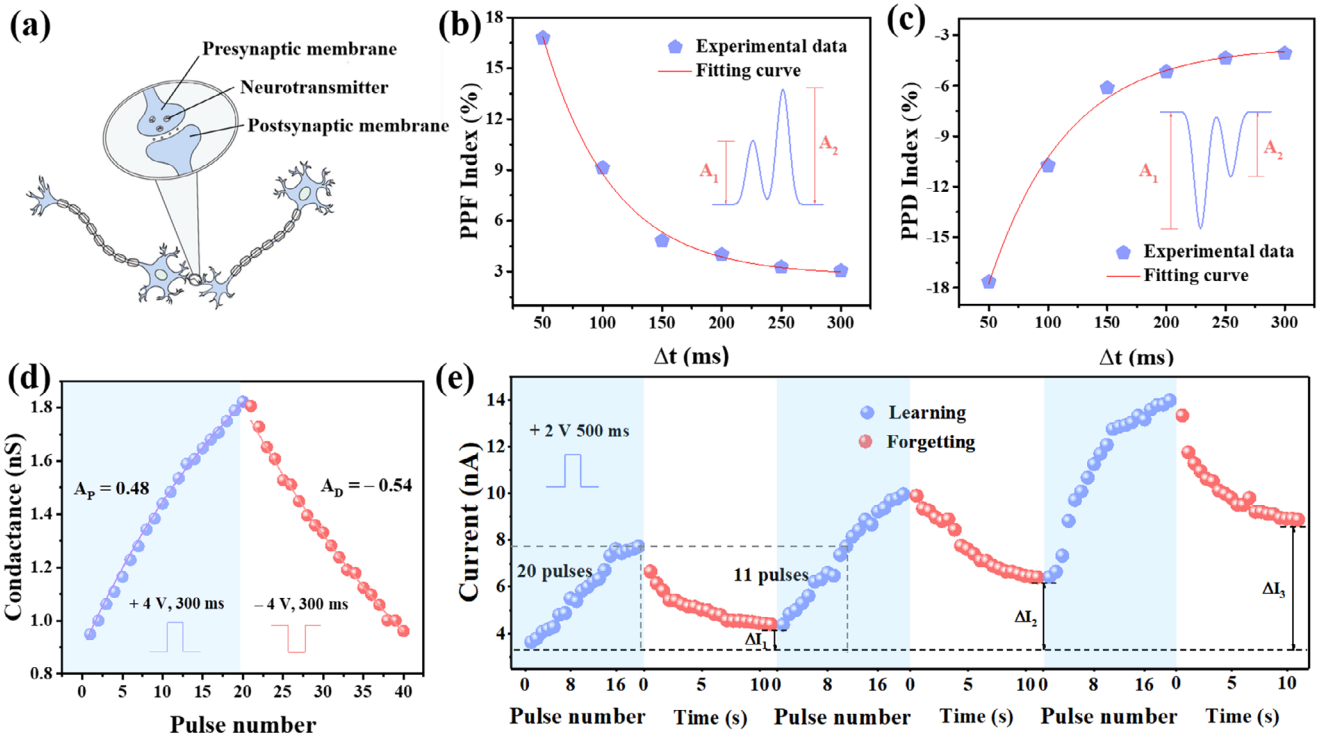

FIGURE 4 | Synaptic behaviors of MPNF-based memristors. (a) Schematic of a biological synapse. (b) The PPF function is stimulated by positive pulses. (c) The PPD function is stimulated by negative pulses. (d) Typical LTP and LTD functions. (e) Three cycles of the "learning-forgetting" process.

where G_{max} (G_{min}) is the maximum (minimum) conductance, A_P (A_D) is the nonlinear parameters of conductance update for LTP (LTD), and P_{max} is the maximum number of voltage pulses. The nonlinear parameters for LTP and LTD can be calculated to be 0.48 and −0.54, respectively, suggesting high linearity of the weight update for the LTP and LTD [37]. Furthermore, the learning-forgetting experience can be emulated by utilizing the MPNF memristors, as shown in Figure 4e. When stimulated by 20 positive voltage pulses (V = 2 V, W = 0.5 s, and Δt = 0.05 s), the device exhibits a stable increase in response current from 3.63 to 7.72 nA, which corresponds to the learning process. Then, the current is gradually decreased to 4.39 nA after removing the voltage pulses, which is the forgetting process. In the subsequent relearning process, only 11 pulses are needed to achieve the same current level as in the first learning process, where 20 pulses are employed. This is analogous to the relearning experience with less time to achieve the same cognitive level as the first learning [38]. Moreover, after continuous stimulation of the pulse sequence, the remaining current after the decay process can be continuously increased, that is, $\Delta I_3 > \Delta I_2 > \Delta I_1$, indicating that the cognitive level can be improved through constant learning.

For neuromorphic computing, the accuracy of recognition is highly dependent on the linearity of the weight update in LTP and LTD and the repeatability of the LTP/LTD cycles [39, 40]. Figure 5a demonstrates 10 sets of LTP and LTD cycles with good linearity and symmetry in each cycle and good repeatability between each cycle. The retention characteristics for multilevel conductance states in the synaptic plasticity are measured for 1000 s, as shown in Figure S12. Although fluctuations and overlaps for adjacent conductance states can be observed during retention tests, the fluctuations are well confined, and the conductance states show the LTP trend as the pulse number increases. Then, a three-layer artificial neural network (ANN) can be simulated through the CrossSim platform with the program code written in Python according to the backpropagation algorithm [41, 42], which can be used for handwritten digit recognition, as demonstrated in Figure 5b. The synaptic memristors are simulated in an $N \times M$ crossbar array for the ANN, as shown in Figure 5c. The small image with 8 × 8 pixels and the large one with 28 × 28 pixels are used for training and testing of the digit recognition [42]. The recognition accuracy of handwritten digits as a function of the training epochs is shown in Figure 5d,e. After 40 training epochs, the recognition accuracy for small images can be maintained at 95.2%, which is very close to the ideal value of 96.7%. The recognition accuracy for a large image can reach up to 91.5%. Furthermore, to evaluate the effect of the cell-to-cell variations on the CrossSim simulations, the LTP/LTD functions from five typical MPNF memristors are employed to perform the handwritten digit recognition simulation [43]. The LTP/LTD variations of the five typical devices with seven cycles of LTP and LTD for each memristor are shown in Figure 5f. The recognition accuracy can reach up to 92.36%, even after considering the cell-to-cell variations, as shown in Figure 5g. Such simulation results indicate potential applications of our MPNF memristors for future neuromorphic computing.

Moreover, we compare the key parameters of our memristors with some published works based on organic materials, including the ON/OFF ratio, SET and RESET voltages, endurance and retention performance, multilevel storage, nonlinear parameter, and recognition accuracy, as shown in Table S2. Our memristors possess comparable RS behaviors and synaptic functions to

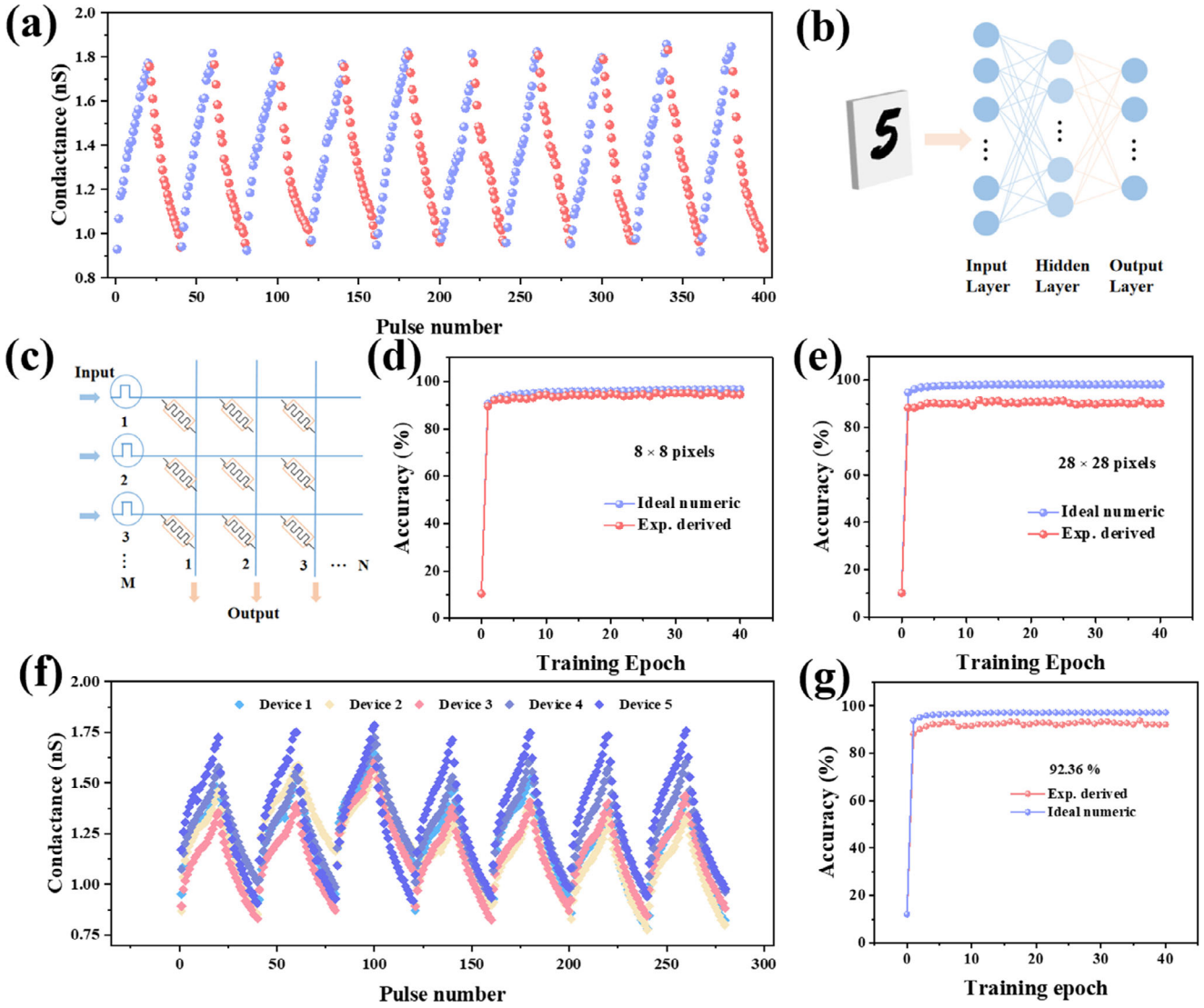

FIGURE 5 | Neuromorphic computing based on the synaptic memristors. (a) 10 sets of LTP/LTD cycles. (b) Schematic of a three-layer artificial neural network for image recognition. (c) Schematic of the crossbar array used for matrix operations. Recognition accuracy of the artificial neural network as a function of the training epoch for (d) a small image of 8 × 8 pixels and (e) a large image of 28 × 28 pixels. (f) The LTP/LTD cycles for five typical synaptic memristors. (g) The recognition accuracy after considering the device-to-device variations.

recently published ones. Furthermore, our organic materials in memristive devices offer significant advantages over inorganic counterparts owing to their cost-effectiveness, low-temperature processing, tunable molecular structures, and mechanical flexibility. Then, the flexibility of the device is examined on the flexible PET substrate, as shown in Figure S13. The memristor still demonstrates good LTP and LTD behaviors even after 1000 bending times and bent at the bending radius of 15, 10, and 5 mm, respectively, suggesting good flexibility for our synaptic memristors.

Furthermore, the decimal arithmetic can be performed based on the good linear relationship between the device conductance and the number of voltage pulses [44, 45]. Such decimal arithmetic can also demonstrate a proof of concept for designing new arithmetic operations beyond the binary system. [46, 47] As shown in Figures 2d–f, the device current can be continuously modulated by the consecutive positive and negative scanning voltages, suggesting the potential of high linearity in potentiation and depression. Figure S14 shows the nearly linear relationship between the device currents read at ±1 V and voltage sweeping numbers, suggesting that the memristor has good linear modulation capability in both pulse and DC modes, as well as good potential for applications in decimal arithmetic. Based on the fabricated synaptic memristors, positive pulses that linearly increase the device current can be utilized to implement addition operations, while negative pulses that linearly decrease the device current can be used for subtraction operations in decimal arithmetic. Figure 6 shows the implementation of decimal arithmetic of addition, subtraction, multiplication, and division operations. The percent change of the device current (PCDC) was recorded to count the quantity of input pulses. In order to achieve accurate arithmetic operations, the 12 − 12 = 0 operation is performed to calibrate the current variation of the memristor, as shown in Figure 6a. When 12 consecutive positive pulses ($V = 4$ V, $W = 0.5$ s) are employed to stimulate the device, the PCDC with respect to

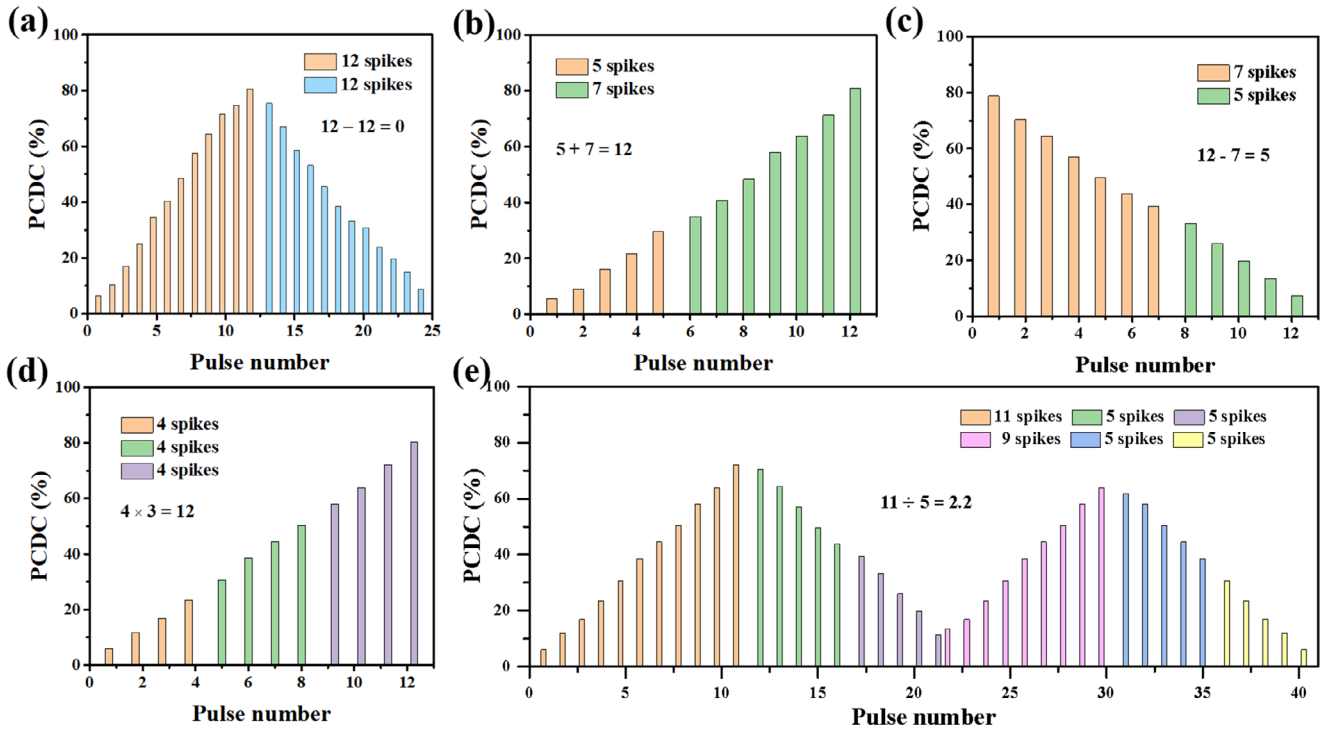

FIGURE 6 | Emulation of decimal arithmetic of addition, subtraction, multiplication, and division operations based on the synaptic memristors. (a) Calibration with the operation 12 – 12 = 0 for accurate decimal arithmetic. (b) The addition operation of 5 + 7 = 12. (c) Subtraction operation of 12 – 7 = 5. (d) Multiplication operation of 4 × 3 = 12. (e) Division operation of 11/5 = 2.2.

the initial current gradually increases to 80%. This PCDC value is defined as the decimal number 12, and the numbers between 0 and 12 can accordingly be indexed proportionally. Then, 12 negative pulses ($V = -4$ V, $W = 0.5$ s) are applied to the device. The PCDC returns to 0%, which executes a subtraction operation of 12 – 12 = 0 as well as the calibration for arithmetic operations. By utilizing the initial calibration, the cell-to-cell variations can be ruled out. For the addition operation of 5 + 7 = 12, a sequence of five pulses (4 V, 0.5 s) is applied to the device first, followed by a sequence of seven pulses (4 V, 0.5 s) after an interval of 10 s (Figure 6b). The PCDC can reach 80%, indicating the addition operation of 5 + 7 = 12. Furthermore, the commutative law of the addition operation can be verified by reversing the order of the two pulse sequences, that is, 7 + 5 = 5 + 7 = 12, as shown in Figure S15a. For the subtraction operation of 12 – 7 = 5, a sequence of seven negative pulses (−4 V, 0.5 s) followed by a sequence of five negative pulses (−4 V, 0.5 s) after an interval of 10 s is employed to stimulate the device with a PCDC value of 80%, as shown in Figure 6c. The PCDC value of the device can be reduced from 80% to 0%, indicating the subtraction operation of 12 – 7 = 5. Then, consecutive addition operations are used to implement multiplication. Take the operation of 4 × 3 = 12 as an example; three pulse sequences with four voltage pulses in each sequence (4 V, 0.5 s) are used to stimulate the device, achieving 80% of the PCDC value (Figure 6d). Moreover, the commutative law of the multiplication operation of 4 × 3 = 3 × 4 is demonstrated in Figure S15b. Furthermore, the division operation is implemented by combining the subtraction and addition operations. For the operation of X/Y, the subtraction operation "$X - Y - Y \ldots$" will be continued until the remainder (r) is less than Y. The quotient is defined as the number of the implemented subtraction operations. Then the r is performed, the addition operation of adding $r \times 9$ for the subsequent subtraction of Y. The subtraction-addition-subtraction operation will be continued until the r is 0. For the division operation of 11/5 = 2.2, a sequence of 11 positive pulses (4 V, 0.5 s) followed by two sequences of five negative pulses (−4 V, 0.5 s) is employed to stimulate the device, corresponding to the subtraction operation of 11 – 5 – 5, as shown in Figure 6e. The quotient is 2, and the r is 1. Then, nine positive pulses are employed to perform the addition operation of 1 + 1 × 9. After the addition operation, two sequences with five negative pulses (−4 V, 0.5 s) in each are used to perform the subtraction operation of 10 – 5 – 5, inducing that the PCDC value returns to 0%. Therefore, the quotient for the division operation of 11/5 is 2.2. All these data indicate that the fabricated MPNF memristors can be used for implementing decimal arithmetic.

3 | Conclusions

In summary, we propose a novel design strategy of introducing different substituents to serve as electron acceptors or donors to achieve high-performance digital RS behaviors for multilevel storage or outstanding analog RS behaviors for synaptic memristors. Based on the furan-annulated naphthalenes, we design and synthesize an organic semiconductor of TPNF by introducing the substituent of trifluoromethyl on the phenyl ring to form D–A pairs, demonstrating typical bipolar digital RS behaviors with multilevel storage characteristics. On the other hand, MPNF with only electron-donor units demonstrates analog RS behaviors and excellent synaptic functions of PPF, PPD, LTP, and LTD. More importantly, the memristors exhibit high conductance modulation linearity in LTP and LTD, which is highly desirable for future

neuromorphic computing. Simulation results demonstrate that the MPNF memristors with high linearity of conductance modulation are completely capable of recognizing digit images with high accuracy and performing decimal arithmetic of addition, subtraction, multiplication, and division operations. This study indicates that the strategy of introducing different substituents is a feasible way to modulate RS properties, and our well-designed organic semiconductors are suitable for applications in multilevel storage and neuromorphic computing.

4 | Experiments Section

The detailed synthesis routine is shown in Figure S1, Supporting Information. Then, the organic thin films were deposited by the thermal evaporation method under the vacuum condition of 6×10^{-3} Pa at 120°C on SiO_2/Si substrates for characterization and ITO-coated PET substrates for memristor fabrication. The synthesized powder and deposited thin films were characterized by NMR, XRD, and Raman spectroscopy. The NMR spectra were obtained on an Avance NEO 600 M spectrometer. A raman spectroscope (Renishaw/inVia, UK) with a 532 nm laser and XRD (Rigaku/MiniFlex, Japan) were employed to characterize the organic materials. The surface morphology and thickness of the organic film were determined by AFM (Bruker/Size Edge, US) and SEM (Seiss/Sigma 500, UK). Moreover, a UV–VIS spectrophotometer (UV2310II) and a UPS (Thermo ESCALAB 250XI) were employed to further characterize the two organic materials. For measurements of the RS behaviors, Pt electrodes with a thickness of about 100 nm were prepared through the sputtering technique by using a well-designed shadow mask. All electrical performance tests were performed with a four-probe station system equipped with a double-channel source meter (Keithley 2636B).

Acknowledgments

This work was supported by grants from the National Natural Science Foundation of China (Nos. 62474118, 52233014, and 62411560160), the Sichuan Science and Technology Program (No. 2022ZYD0041), and PolyU grants (1-W22S and 1-CE0H). D.W. and J.Y. contributed equally to this work.

Conflicts of Interest

The authors declare no conflicts of interest.

References

1. H. Xie, S. Chen, X. Yang, et al., "Printed On-Chip Perovskite Heterostructure Arrays for Optical Switchable Logic Gates," *Advanced Materials* 36 (2024): e2404740.

2. Z. Y. He, T. Y. Wang, J. L. Meng, et al., "CMOS Back-End Compatible Memristors for In Situ Digital and Neuromorphic Computing Applications," *Materials Horizons* 8 (2021): 3345–3355.

3. P. R. S. Reddy, V. R. Nallagatla, Y. A. Kumar, et al., "Enhanced Resistive Switching Properties of HfAlOx/ZrO_2-Based RRAM Devices," *Progress in Natural Science: Materials International* 32 (2022): 602–607.

4. F. Guo, M. Song, M. C. Wong, et al., "Multifunctional Optoelectronic Synapse Based on Ferroelectric Van der Waals Heterostructure for Emulating the Entire Human Visual System," *Advanced Functional Materials* 32 (2021): 2108014.

5. S. Park, Z. Liao, B. Ibarlucea, et al., "Two-Dimensional Boronate Ester Covalent Organic Framework Thin Films With Large Single Crystalline Domains for a Neuromorphic Memory Device," *Angewandte Chemie* 59 (2020): 8218–8224.

6. A. Bala, A. Sen, J. Shim, et al., "Back-End-of-Line Compatible Large-Area Molybdenum Disulfide Grown on Flexible Substrate: Enabling High-Performance Low-Power Memristor Applications," *ACS Nano* 17 (2023): 13784–13791.

7. Y. Liu, X. Zhou, H. Yan, et al., "Highly Reliable Textile-Type Memristor by Designing Aligned Nanochannels," *Advanced Materials* 35 (2023): 2301321.

8. X. N. Zhao, J. Q. Xu, D. Xie, et al., "Natural Acidic Polysaccharide-Based Memristors for Transient Electronics: Highly Controllable Quantized Conductance for Integrated Memory and Nonvolatile Logic Applications," *Advanced Materials* 33 (2021): 2104023.

9. Y. Tao, H. Liu, H. Y. Kong, et al., "Resistive Memristors Using Robust Electropolymerized Porous Organic Polymer Films as Switchable Materials," *Journal of the American Chemical Society* 146 (2024): 16511–16520.

10. H. Li, B. Xiong, J. Xu, et al., "Chiral Transfer-Dictated Self-Assembly of Chiral Block Copolymers," *Aggregate* 2 (2021): e122.

11. S. Goswami, S. Goswami, and T. Venkatesan, "An Organic Approach to Low Energy Memory and Brain Inspired Electronics," *Applied Physics Reviews* 7 (2020): 021303.

12. K. H. Liao, P. X. Lei, M. L. Tu, et al., "Memristor Based on Inorganic and Organic Two-Dimensional Materials: Mechanisms, Performance, and Synaptic Applications," *ACS Applied Materials & Interfaces* 13 (2021): 32606–32623.

13. A. Bandyopadhyay, S. Sahu, and M. Higuchi, "Tuning of Nonvolatile Bipolar Memristive Switching in Co(III) Polymer With an Extended Azo Aromatic Ligand," *Journal of the American Chemical Society* 133 (2011): 1168–1171.

14. D. Li, B. Zhang, C. Zhu, et al., "In-Situ Growing D–A Polymer From the Surface of Reduced Graphene Oxide: Synthesis and Nonvolatile Ternary Memory Effect," *Carbon* 143 (2019): 851–858.

15. Y. Tao, H. Liu, H. Y. Kong, et al., "Electrochemical Preparation of Porous Organic Polymer Films for High-Performance Memristors," *Angewandte Chemie* 61 (2022): 12432.

16. R. Gayathri, V. M. Angela, P. Devibala, et al., "Tailoring the Resistive Switching WORM Memory Behavior of Functionalized Bis(Triphenylamine)," *ACS Applied Materials & Interfaces* 15 (2023): 23546–23556.

17. Y. Li, Q. Qian, S. Ling, et al., "A Benzothiadiazole-Containing Π-Conjugated Small Molecule as Promising Element for Nonvolatile Multilevel Resistive Memory Device," *Journal of Solid State Chemistry* 294 (2021): 121850.

18. X. Zhang, H. Chen, S. Cheng, et al., "Tunable Resistive Switching in 2D MXene Ti_3C_2 Nanosheets for Non-Volatile Memory and Neuromorphic Computing," *ACS Appl Mater Interfaces* 14 (2022): 44614–44621.

19. W. Wei and X. Wang, "Ion-Specific Effects in Confined Nanochannels and Neural Network," *Aggregate* 4 (2023): e302.

20. Q. Q. Zeng, Y. Q. Wang, L. Cheng, et al., "Regiocontrolled Annulation of Benzocyclobutenols With Alkynes," *Organic Letters* 24 (2022): 3058–3063.

21. P. Matczak, S. Domagała, W. Weigand, et al., "A Comparative Analysis of UV–Vis Transitions in Hetaryl and Ferrocenyl Thioketones," *Chemical Physics* 570 (2023): 111901.

22. Z. Zhao, M. E. El-Khouly, Q. Che, et al., "Redox-Active Azulene-Based 2D Conjugated Covalent Organic Framework for Organic Memristors," *Angewandte Chemie* 62 (2023): e202217249.

23. D. Insuasty, L. Cabrera, A. Ortiz, et al., "Synthesis, Photophysical Properties and Theoretical Studies of New Bis-Quinolin Curcuminoid Bf_2-Complexes and Their Decomplexed Derivatives," *Spectrochimica Acta, Part A: Molecular and Biomolecular Spectroscopy* 230 (2020): 118065.

24. X. Zhang, Q. Zhou, Y. Huang, et al., "Contrastive Analysis of the Raman Spectra of Polychlorinated Benzene: Hexachlorobenzene and Benzene," *Sensors* 11 (2011): 11510–11515.

25. M. Makela, P. Gordon, D. Tu, et al., "Benzene Derivatives Analysis Using Aluminum Nitride Waveguide Raman Sensors," *Analytical Chemistry* 92 (2020): 8917–8922.

26. T. S. Vo and T. T. B. C. Vo, "Surface Characterization of Polyimide and Polyethylene Terephthalate Membranes Toward Plasma and Uv Treatments," *Progress in Natural Science: Materials International* 32 (2022): 314–327.

27. Z. Li, E. Y.-H. Hong, and C.-T. Poon, "Synthesis, Characterization, Supramolecular Self-Assembly, and Organic Resistive Memory Applications of BODIPY Derivatives," *ACS Materials Letters* 5 (2023): 909–919.

28. J. Yang, W. Wang, Y. Liu, et al., "Thickness Dependence of the Charge-Density-Wave Transition Temperature in VSe_2," *Applied Physics Letters* 105 (2014): 063109.

29. S. Y. Kim, J. M. Yang, E. S. Choi, et al., "Layered $(C_6H_5CH_2NH_3)_2CuBr_4$ Perovskite for Multilevel Storage Resistive Switching Memory," *Advanced Functional Materials* 30 (2020): 2002653.

30. J. Xu, X. Zhao, Z. Wang, et al., "Biodegradable Natural Pectin-Based Flexible Multilevel Resistive Switching Memory for Transient Electronics," *Small* 15 (2019): 1803970.

31. C. Zhang, Y. Li, F. Yu, et al., "Visual Growth of Nano-HOFs for Low-Power Memristive Spiking Neuromorphic System," *Nano Energy* 109 (2023): 108274.

32. U. Jung, M. Kim, J. Jang, et al., "Formation of Cluster-Structured Metallic Filaments in Organic Memristors for Wearable Neuromorphic Systems With Bio-Mimetic Synaptic Weight Distributions," *Advancement of Science* 11 (2024): 2307494.

33. J. S. Najem, G. J. Taylor, R. J. Weiss, et al., "Memristive Ion Channel-Doped Biomembranes as Synaptic Mimics," *ACS Nano* 12 (2018): 4702–4711.

34. P. Lei, H. Duan, L. Qin, et al., "High-Performance Memristor Based on 2D Layered BiOI Nanosheet for Low-Power Artificial Optoelectronic Synapses," *Advanced Functional Materials* 32 (2022): 2201276.

35. W. Wang, S. Gao, Y. Li, et al., "Artificial Optoelectronic Synapses Based on TiN_xO_{2-x}/MoS_2 Heterojunction for Neuromorphic Computing and Visual System," *Advanced Functional Materials* 31 (2021): 2101201.

36. S. Cheng, L. Zhong, J. Yin, et al., "Controllable Digital and Analog Resistive Switching Behavior of 2D Layered WSe_2 Nanosheets for Neuromorphic Computing," *Nanoscale* 15 (2023): 4801–4808.

37. W. Xie, Y. Zhong, D. Wang, et al., "Co-Existence of Digital and Analog Resistive Switching in 2D Layered BiOI Nanosheets for Synaptic Applications," *Materials & Design* 234 (2023): 112367.

38. Z. Q. Wang, H. Y. Xu, X. H. Li, et al., "Synaptic Learning and Memory Functions Achieved Using Oxygen Ion Migration/Diffusion in an Amorphous InGaZnO Memristor," *Advanced Functional Materials* 22 (2012): 2759–2765.

39. J. Sun, S. Oh, Y. Choi, et al., "Optoelectronic Synapse Based on IGZO-Alkylated Graphene Oxide Hybrid Structure," *Advanced Functional Materials* 28 (2018).

40. Y. X. Hou, Y. Li, Z. C. Zhang, et al., "Large-Scale and Flexible Optical Synapses for Neuromorphic Computing and Integrated Visible Information Sensing Memory Processing," *ACS Nano* 15 (2020): 1497–1508.

41. E. J. Fuller, F. E. Gabaly, F. Léonard, et al., "Li-Ion Synaptic Transistor for Low Power Analog Computing," *Advanced Materials* 29 (2016): 1604310.

42. Z. Dang, F. Guo, H. Duan, et al., "Black Phosphorus/Ferroelectric P(VDF-TrFE) Field-Effect Transistors With High Mobility for Energy-Efficient Artificial Synapse in High-Accuracy Neuromorphic Computing," *Nano Letters* 23 (2023): 6752–6759.

43. S. T. Yang, X. Y. Li, T. L. Yu, et al., "High-Performance Neuromorphic Computing Based on Ferroelectric Synapses With Excellent Conductance Linearity and Symmetry," *Advanced Functional Materials* 32 (2022): 2202366.

44. Z. Peng, Z. Cheng, S. Ke, et al., "Flexible Memristor Constructed by 2D Cadmium Phosphorus Trichalcogenide for Artificial Synapse and Logic Operation," *Advanced Functional Materials* 33 (2022): 2211269.

45. X. Yan, H. He, G. Liu, et al., "A Robust Memristor Based on Epitaxial Vertically Aligned Nanostructured $BaTiO_3-CeO_2$ Films on Silicon," *Advanced Materials* 34 (2022): 2110343.

46. B. Zhang, F. Fan, W. Xue, et al., "Redox Gated Polymer Memristive Processing Memory Unit," *Nature Communications* 10 (2019): 736.

47. T. Zeng, S. Shi, k. Hu, et al., "Approaching the Ideal Linearity in Epitaxial Crystalline-Type Memristor by Controlling Filament Growth," *Advanced Materials* 36 (2024): 2401021.

Supporting Information

Additional supporting information can be found online in the Supporting Information section.

Supporting Information file 1: agt270095-sup-0001-SuppMat.pdf